This document is confidential and is proprietary to the American Chemical Society and its authors. Do not copy or disclose without written permission. If you have received this item in error, notify the sender and delete all copies.

Hydrogen-Type Binding Sites in Carbonaceous Electrodes for Rapid Lithium Insertion

Journal:	*ACS Applied Materials & Interfaces*
Manuscript ID	am-2023-05047h.R2
Manuscript Type:	Article
Date Submitted by the Author:	n/a
Complete List of Authors:	McGlamery, Devin; Montana State University, Chemistry & Biochemistry McDaniel, Charles; Montana State University, Chemistry & Biochemistry Xu, Wei; Montana State University System, Chemistry and Biochemistry Stadie, Nicholas; Montana State University System, Chemistry and Biochemistry

SCHOLARONE™
Manuscripts

Hydrogen-Type Binding Sites in Carbonaceous Electrodes for Rapid Lithium Insertion

Devin McGlamery, Charles McDaniel, Wei Xu, and Nicholas P. Stadie*

Department of Chemistry & Biochemistry, Montana State University, Bozeman, Montana 59717, United States

*Email: nstadie@montana.edu

Abstract: Direct pyrolysis of coronene at 800 °C produces low surface area, nanocrystalline graphitic carbon containing a uniquely high content of a class of lithium binding sites referred to herein as "hydrogen-type" sites. Correspondingly, this material exhibits a distinct redox couple under electrochemical lithiation that is characterized as intermediate-strength, capacitive lithium binding, centered at ~0.5 V vs. Li/Li^+. Lithiation of hydrogen-type sites is reversible and electrochemically distinct from capacitive lithium adsorption and from intercalation type binding between graphitic layers. Hydrogen-type site lithiation can be fully retained even up to ultrafast current rates (e.g., 15 A g^{-1}, ~40 C) where intercalation is severely hampered by ion desolvation kinetics; at the same time, the bulk nature of these sites does not require a large surface area and only minimal electrolyte decomposition occurs during the first charge/discharge cycle, making coronene-derived carbon an exceptional candidate for high-energy density battery applications.

Keywords: graphitic, carbon, lithium-ion, anode, pseudocapacitive, insertion mechanism, rapid charging, energy storage

INTRODUCTION

Graphite remains the de facto anode material for lithium-ion batteries (LIBs) since it was introduced into the commercial market in the 1990s,[1,2] favored for its low operating potential of ~0.1 V vs. Li/Li^+, high reversible capacity (LiC_6, 372 mAh g^{-1}), and admirable safety compared to metallic lithium.[3–5] However, the demands of next generation LIBs require faster charging than is accessible to the intercalation chemistry native to graphite-based LIB anodes.[6] At charging rates above 1 C (i.e., a 60 min charging time), the reversible capacity of crystalline graphite is precipitously reduced owing to sluggish desolvation kinetics of lithium from within standard liquid carbonate electrolytes at the surface of the graphite anode.[7–11] Recent work has shown that the rate capability is correlated with specific properties of the chosen type of graphite, including such properties as crystallite size, particle size, and content and type of lattice imperfections; reasonable capacity can be retained in high-performance variants up to roughly 4 C (i.e., a 15 min charging time) but requires a precisely tuned, anode-limited full-cell.[12] Other methods have been shown to elevate the rate capability of graphite through modification strategies such as laser patterning and nanosizing, increasing the complexity of electrode fabrication.[13–16] On the other hand, high surface area porous carbon materials can effectively store lithium under ultrafast charging rates via the capacitive adsorption of ions and formation of an electric double-layer at their surfaces.[17] The reversible capacity of these materials increases with surface area to far higher than 372 mAh g^{-1};[18–20] however, due to decomposition of electrolyte and the resulting formation of solid electrolyte interphase (SEI) on all exposed surfaces of the electrode, a massive irreversible consumption of electrolyte occurs during the first cycle in standard Li-ion electrolytes, prohibitive to their use in commercial battery applications.[21]

Dahn and coworkers have noted a third type of lithium interaction within carbonaceous materials containing a significant amount of hydrogen.[22,18] This type of binding is categorized as distinct from strongly bound intercalation and weakly bound capacitive ion adsorption. A distinct charge storage

mechanism was surmised to result, via charge transfer between lithium guests and hydrogen terminations at edges in the carbon structure: i.e., the formation of dative covalent bonds.[22] Hence, this type of charge storage would be expected to be faradaic, but was not definitively characterized. The general effect of hydrogen content on lithium uptake was explored in detail by Dahn and coworkers by lithiation of the pyrolysis products of petroleum pitches, polyvinyl chloride, and polyvinylidene fluoride between 550-1000 °C.[23] These experiments exhaustively supported an increasing reversible lithiation capacity with increasing hydrogen content, and further evidenced atomistic rearrangement of the edge-site carbon upon lithiation/delithiation, as observed by a large voltage hysteresis between the charge and discharge profiles. Interestingly, little more remains understood, even over 20 years later, about the specific atomistic mechanism associated with this type of lithium binding. A hurtle in characterizing any kind of lithiation site or charge storage mechanism lies in obtaining a material which exhibits that site or mechanism in abundance; the work presented herein reveals that coronene-derived carbon pyrolyzed at 800 °C is such a material for hydrogen-type lithiation sites.

RESULTS AND DISCUSSION

In this work, we hypothesized that the partial pyrolysis of a large polyaromatic hydrocarbon (PAH) precursor would result in the synthesis of a low surface area, nanocrystalline graphitic carbon containing a high content of confined hydrogen edge sites between adjacent precursor molecules. A series of PAHs (benzene, naphthalene, pyrene, and coronene) were explored to determine the effects of precursor size and hydrogen content on the structure and composition of the pyrolysis product, and especially on its number and type of lithiation sites available for electrochemical ion storage. The model compound for further in-depth study was obtained via the pyrolysis of neat coronene ($C_{24}H_{12}$) under closed conditions at 800 °C, the product of which is referred to herein as Cor800. While coronene exhibits the lowest initial hydrogen content of all PAHs explored herein, its large size encourages a significant role for precursor stacking prior to and during pyrolysis and reduces the likelihood of perfect tiling of the 2D graphitic plane.

Interestingly, upon electrochemical lithiation, a distinct type of lithiation site was observed in high quantity in Cor800 that cannot be classified as either faradaic intercalation within the graphitic layers or as capacitive formation of an electric double layer at the particle surfaces. This was confirmed by systematic comparison with several benchmark types of carbonaceous electrode materials with well-resolved carbon structures: crystalline graphite (AG20) with almost exclusively interlayer-type lithiation sites, high surface-area zeolite-templated carbon (ZTC) with exclusively surface-type lithiation sites, and a standard hard carbon (Super P) that exhibits (widely-spaced) interlayer sites as well as a significant content of surface sites. Scanning electron micrographs of Cor800 and the three benchmark materials of comparison are shown in **Figure 1** as indicative of their complementary structure and composition; proposed atomistic depictions of the same materials are shown in the Supporting Information. The novel sites in Cor800, referred to hereafter as "hydrogen-type" sites, were thoroughly characterized using a suite of electrochemical techniques and could still be lithiated reversibly even at ultrafast charging rates up to 40 C (corresponding to a 90 s charging time).

The structure of Cor800 was first investigated using powder X-ray diffraction (XRD) and Raman spectroscopy, for comparison to the three benchmark standards (**Figures 1c** and **1f**). Cor800 exhibits a broad peak indexed as the (002) reflection of the AB-stacked graphite unit cell, corresponding to an interlayer spacing (d_{002}) of 3.42 Å and an average crystallite size along the c-axis (L_c) of 22 Å, ~6 graphitic layers. This contrasts with the XRD pattern of AG20 which exhibits a narrow (002) reflection corresponding to a d_{002} of 3.35 Å and an average L_c of 314 Å (~94 graphitic layers). AG20 is therefore a far more crystalline graphite than Cor800, though its small particle size of 15.2 ± 3.5 μm permits a relatively high rate capability toward lithiation in standard carbonate electrolytes.[12] Super P, a commercial hard carbon, also shows a weak (002) reflection corresponding to an expanded graphitic structure with a d_{002} spacing of 3.54 Å and an L_c of 21 Å (~6 graphitic layers). The final comparison material, ZTC, is a unique, highly porous carbonaceous framework solid with no (002) peak related to graphitic stacking.[24] The long-range order

present in the atomistic structure of ZTC originates from the original faujasite (**FAU**) template; the XRD pattern exhibits an intense (111) reflection at 6.4°, corresponding to a pore-to-pore d-spacing of 14.1 Å and a coherence length of 284 Å (~20 pore-to-pore repeats). Hence, ZTC is a model material for purely capacitive lithium storage since its unique chemical vapor deposition (CVD) synthesis within a microporous zeolite template gives rise to a material that, when templated effectively, cannot have any significant graphitic stacking (all parts of the carbon network are double-sided graphene ribbon fragments).[25]

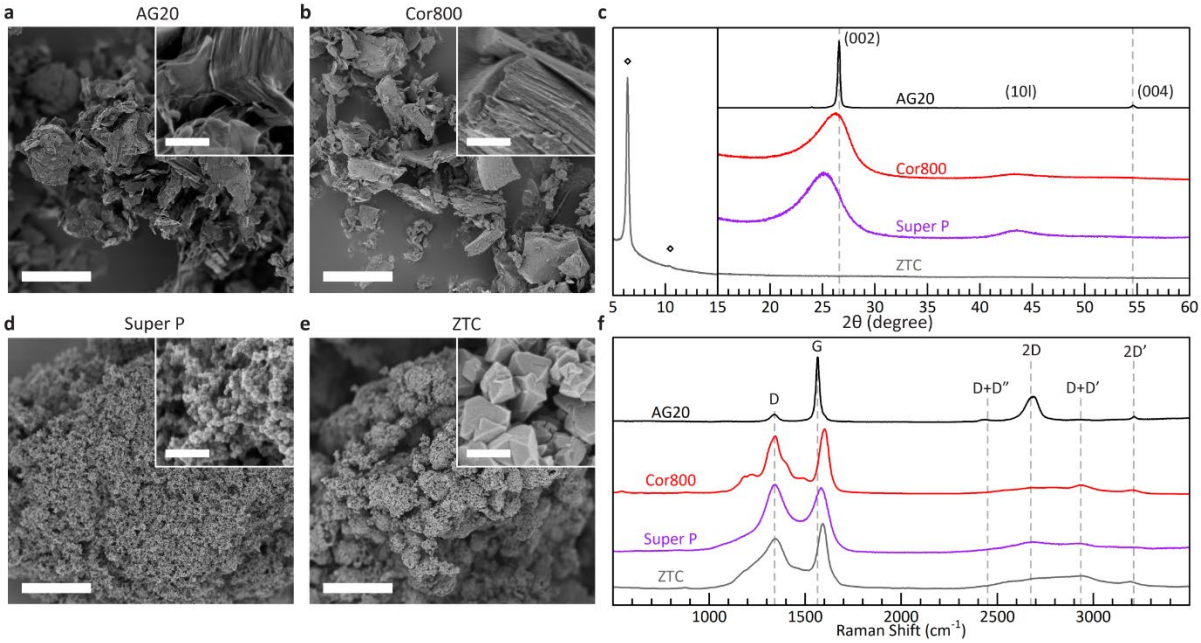

Figure 1. Representative SEM images of (a) graphite (AG20), (b) graphitic carbon with hydrogen-type sites (Cor800), (d) hard carbon (Super P), and (e) ordered porous carbon with no stacking (ZTC). The main image in each panel shows a 20 µm scale bar, and the inset shows a 500 nm scale bar. (c) XRD patterns of AG20, Cor800, Super P, and ZTC with the graphite (002) and (004) reflections indicated as dashed gray lines. The (111) and (220) reflections characteristic of the cubic pore-to-pore ordering in ZTC are indicated with open diamonds. (f) Raman spectra of AG20, Cor800, Super P, and ZTC, collected using a 532 nm excitation source.

Raman spectroscopy reveals additional information about the complementary structural features of Cor800 as compared to AG20, Super P, and ZTC, as shown in **Figure 1f**. All four materials exhibit the usual features of the in-plane structure associated with graphite/graphene (the regime shown relates exclusively to in-plane phonons): the G and D modes, and their overtones and other defect-induced features.[26,27] The Raman spectrum of Cor800 exhibits a prominent G mode that is seemingly shifted to higher frequency (1600 cm^{-1}) than that of crystalline graphite (1564 cm^{-1}), indicating the significant presence of the defect induced D' mode (typically found between 1700-1840 cm^{-1}), not the actual change in frequency of G. This specifically signals the presence of electron hole scattering sites in Cor800, which can also be seen in Super P and ZTC. While Cor800, Super P, and ZTC all exhibit a broad D mode, Cor800 exhibits some unique identifiable features on both shoulders of the D mode. The two features on the low-frequency shoulder at 1182 cm^{-1} and 1285 cm^{-1} correspond to C–H bending modes of armchair and zigzag edges, respectively. The two features on the high frequency shoulder of the D mode at 1395 cm^{-1} and 1462 cm^{-1} correspond to 5,6-ring carbon stretching modes that result from the fusion of coronene molecules during pyrolysis.[28] Thus, Cor800 contains a significant amount of C–H edge character within the crystallites and highly imperfect in-plane bonding. As evidenced by N_2 adsorption studies at 77 K, Cor800 has a low surface area of only ~4 $m^2\ g^{-1}$. However, it also has an exceptionally high content of hydrogen as quantified by combustion analysis (roughly 1 hydrogen per 5 carbon atoms); these results are summarized and compared to the three standard materials in **Table 1**. Hydrogen content is directly correlated with edge sites, a feature that usually gives rise to a higher N_2-accessible surface area. Together with XRD and Raman analysis, this body of evidence reveals a unique, internal content of hydrogen terminations that is buried within the defected graphitic structure of Cor800. In contrast, the D mode of graphite is minimal (as expected for highly crystalline graphite) and that for Super P is expressed as a single peak indicating low hydrogen content and minimal edge character. The D mode of ZTC is broad and exhibits a modulated low frequency shoulder indicating a mixture of armchair and zigzag edges

terminating the network of graphene ribbon-like blades. As expected, the hydrogen content of the three standard materials scales with the N_2-accessible surface area (**Table 1**) indicating that their H-terminations are on "outer surfaces," typical of graphitic and porous carbons.

Table 1. Structural properties of Cor800 and three standard materials of comparison, as determined using XRD, Raman spectroscopy, N_2 adsorption at 77 K, combustion analysis, and electrochemical lithiation.

	XRD			Raman Spectroscopy		N_2 Adsorption	Combustion Analysis	Electrochemical Lithiation
	d_{002} (Å)	L_c (Å)	L_a (Å)	Pos(G) (cm^{-1})	FWHM(G) (cm^{-1})	BET SA ($m^2 g^{-1}$)	H:C (molar ratio)	Total Li Capacity* (mAh g^{-1})
Cor800	3.42	22	18	1600	53	4	0.20	297
AG20	3.35	314	43	1564	20	9	0.00	320
ZTC	-	-	-	1592	60	3330	0.20	255
Super P	3.54	21	41	1583	103	59	0.01	265

* - reversible low-rate (25 mA g^{-1}) GCD capacity, measured as the average of the 15th-20th delithiation cycles

The lithiation of Cor800 was investigated by performing a series of electrochemical experiments in half-cell configuration against lithium metal, in the presence of a standard carbonate-based electrolyte (see the Supporting Information for details). First, cyclic voltammetry (CV) at a low scan rate (0.1 mV s^{-1}) was used to deduce the number and type of lithiation mechanism(s) within Cor800 between 0.01-1.5 V vs. Li/Li^+, by reference to identical experiments using the three standard materials (**Figure 2**, dark purple traces). Similarly to Super P, a portion of the lithiation of Cor800 proceeds by wide-interlayer intercalation, as evidenced by a broad oxidation peak upon delithiation at 0.2 V vs. Li/Li^+. Unlike in graphite (which shows numerous intercalation features associated with staging)[29] this peak is expressed as a broad, single peak in both Cor800 and Super P, and the corresponding reduction peak in both cases is an intense, asymmetric feature at close to the cutoff voltage of 0.01 V vs. Li/Li^+. As expected, no such intercalation features exist for ZTC; instead, a box-like profile is observed as is typical for purely capacitive electrode

materials (Super P too shows a constant current background associated with the formation of a modest electric double layer on its surface area of 60 $m^2 g^{-1}$). However, interestingly, a prominent redox couple is also observed in the profile of Cor800 at around 0.5 V vs. Li/Li^+ that is not observed in any of the standard materials used herein, nor in any other materials in the reported literature. We attribute this feature to the lithiation/delithiation of hydrogen-type sites within the bulk graphitic structure of Cor800. This is consistent with the adsorption/desorption of lithium in Li···H–C environments at zigzag edges, predicted to occur at between 0.49-0.66 V.[30]

To explore the relative rates of lithiation of the three above-identified environments, CV was performed at a wide range of scan rates from 0.1-15 mV s^{-1} (select profiles shown in **Figures 2a-2d**). While the features associated with intercalation broadened significantly and then disappeared as scan rate increased, the box-like profile owing to capacitive lithiation (in Super P and ZTC) and the lithiation event attributed to hydrogen-type sites persisted to extremely high scan rates. The scan rate dependences of these features are summarized in **Figures 2e-2h**. Randles-Ševčik (R-S) analysis was then performed to determine the extent of diffusion limitation associated with each type of lithiation mechanism.[31–33] As expected, the staging phenomena associated with intercalation of highly crystalline AG20 (labeled as O1 to O3-4 for the oxidative peaks and R3-4 for the reductive peaks, where the number indicates the stage of intercalation/deintercalation) exhibit a scan rate dependence characteristic of a faradaic charge transfer event (with an R-S slope of ~0.5 across the entire range of scan rates).[31] All other lithiation events were found to exhibit capacitive or pseudocapacitive lithium binding, with R-S slopes significantly greater than 0.5 and approaching 1 at low scan rates. The redox couple associated with intercalation in Cor800 (labeled as O-I and R-I for oxidation and reduction, respectively) persists with an R-S slope of ~1 up to a scan rate of 1 mV s^{-1} (corresponding to a charge rate of ~2 C), a similar fate as low-stage intercalation in AG20. Beyond 2 C, the CV profile of Cor800 is dominated by the hydrogen-type interaction which persists until the ultrafast scan rate of 15 mV s^{-1} (~40 C), and yields an R-S slope of ~1 between 0.1-1 mV s^{-1},

indicating that there are no diffusion limitations to charge transfer or pseudocapacitance in this process.[33] As the scan rate rises above 1 mV s^{-1}, desolvation becomes a limiting factor for lithiation of the hydrogen-type sites, and the R-S slope significantly decreases (its value is no longer meaningful in this region[31]). This analysis reveals that lithium-binding on hydrogen-type sites is likely based on a rapid redox mechanism referred to as pseudocapacitance.[34]

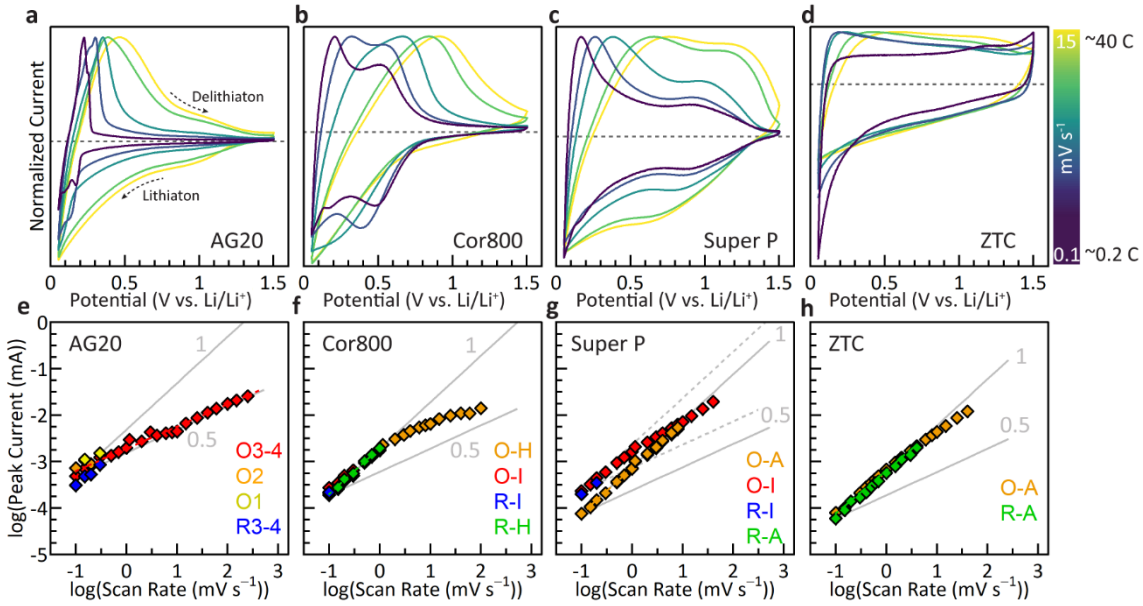

Figure 2. CV analysis of (a,e) AG20, (b,f) Cor800, (c,g) Super P, and (d,h) ZTC at scan rates between 0.1-15 mV s^{-1}. (a-d) Select CV profiles and (e-h) R-S analysis showing the presence of numerous lithiation environments: reductive stage 3-4 intercalation (R3-4), wide interlayer intercalation (R-I), hydrogen-type site binding (R-H), and adsorption (R-A), and oxidative stage 1, 2, or 3-4 intercalation (O1, O2, and O3-4), wide interlayer intercalation (O-I), hydrogen-type site binding (O-H), and adsorption (O-A).

To best quantify the total lithiation capacity of Cor800, galvanostatic charge/discharge (GCD) cycling was performed between 0.01-1.5 V vs. Li/Li^+, as shown in **Figure 3**. The reversible GCD profile of Cor800 at low rate (~0.1 C, **Figure 3a**) shows a similar (negligible) lithiation capacity to AG20 between 1.5-0.75 V vs. Li/Li^+; an indistinct plateau centered at ~0.5 V vs. Li/Li^+ (attributable to hydrogen-type sites) is observed in Cor800, followed by a sloping feature prior to reaching the voltage cutoff, exhibiting a total specific capacity of 300 mAh g^{-1}. A mild voltage hysteresis between charge and discharge is observed,

indicating an overpotential associated with the hydrogen-type and wide interlayer intercalation mechanisms. The magnitude of hysteresis in Cor800 is intermediate between Super P (exhibiting a mild hysteresis) and ZTC (exhibiting a large hysteresis), and not as large as that of high H-content materials reported by Dahn et al.[23] Despite that obvious plateaus are not observed for Cor800 under GCD at low-rate conditions, the GCD profile is generally consistent with the CV profiles shown in **Figure 2** and remains unique compared to the three reference materials herein.

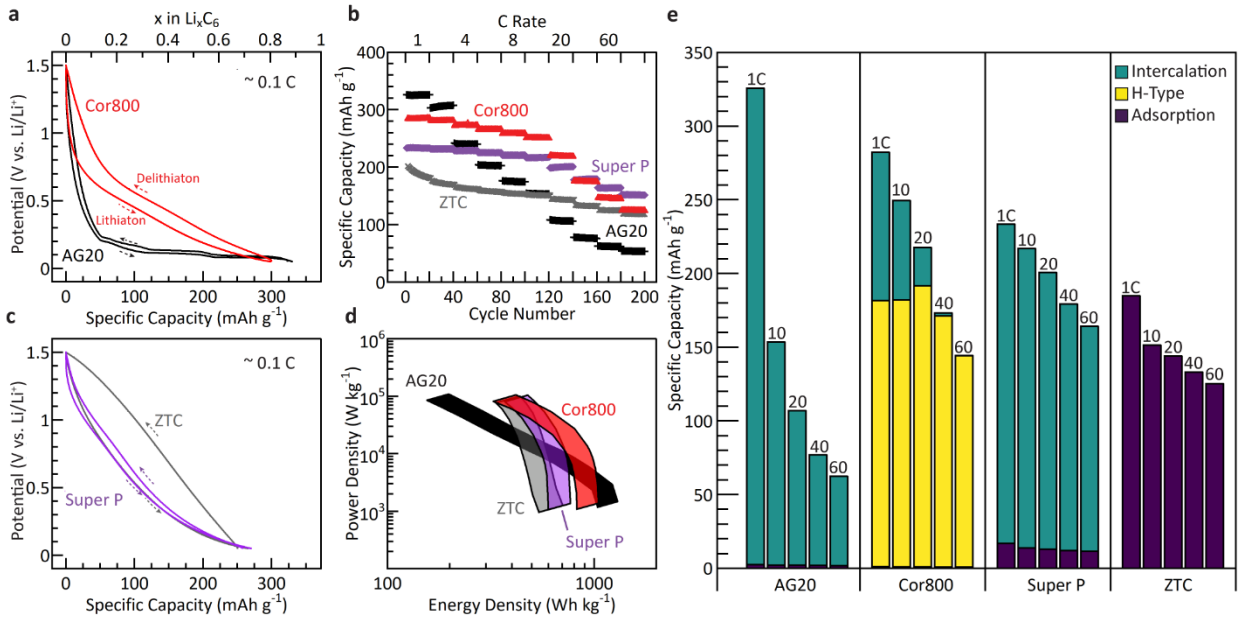

Figure 3. (a, c) Reversible GCD profiles of (a) AG20 and Cor800, and (c) Super P and ZTC at 25 mA g^{-1} (~0.1 C). (b) Cycling stability and rate capability of all materials at current rates between 0.4-30 A g^{-1} (~1-80 C, as shown). (d) Materials-specific Ragone plot assuming use of an anode against a range of standard cathodes (see Supporting Information for details). (e) Allocation of reversible charge storage capacity in all materials as per the type of lithiation environment (indicated by color) as a function of charging rate at select rates of 1 C, 10 C, 20 C, 40 C, and 60 C (indicated above each bar).

The effect of charging rate on capacity retention was then assessed via GCD cycling at increasing rates between 0.4-30 A g^{-1} (~ 0.1-80 C), as shown in **Figure 3b**. A constant current constant voltage (CCCV) charging protocol was employed at each step in the protocol to ensure that all materials were fairly compared (i.e., the total charging time was held to be the same regardless of performance during the CC

phase). These results show, as expected, that while AG20 exhibits the highest capacity at low charging rates, its capacity diminishes significantly at >2 C.[12] Unlike graphite, Cor800 exhibits high capacity retention up to ~10 C, much more akin to Super P and ZTC, both of which benefit from an abundance of surface sites available for capacitive adsorption (which Cor800 does not exhibit). The capacity of Cor800 is the highest among the materials explored herein (under a non-optimized set of cell fabrication conditions, but in an apples-to-apples comparison) until the ultrafast current rate of 60 C is exceeded. The same GCD cycling data are reconfigured as a materials-specific Ragone plot in **Figure 3d**. To convert the average electrochemical potential during discharge to an energy, an estimate of full-cell voltage was made via pairing with a standard cathode material (assuming an average cathode potential of 4.2 or 3.4 V vs. Li/Li^+, respectively). The power density was determined according to the CCCV charging time; further details are provided in the Supporting Information. As noted above, AG20 exhibits the highest energy density and is best suited to low power density applications. Meanwhile, Super P and ZTC show the expected behavior of capacitive materials with nearly constant energy density within the range of power densities explored (up to 100 kW kg^{-1}, per mass of active material only). On the other hand, Cor800 exhibits a high energy density even at relatively high-power densities up to ~10 kW kg^{-1}. The relatively high energy density is attributable to the large number of hydrogen-type sites, while the high-power density is facilitated by only nanoscale crystallinity and the presence of significantly wider interlayer spacing.

In order to decouple the storage mechanisms responsible for the observed reversible capacities of AG20, Cor800, Super P, and ZTC at current rates between 1-60 C, we made a series of reasonable approximations culminating in **Figure 3e**. The total (GCD-derived) discharge capacity at each rate was assessed as a combination of three mechanism types: intercalation (including staging and wide interlayer types), hydrogen-type interactions, and surface adsorption. The surface adsorption capacity was assessed on the basis of the N_2-accessible surface area of each material and calibrated at each rate according to

ZTC. The remaining two mechanisms were distinguished by integration of the CV oxidation profiles (at a scan rate comparable to the given GCD current rate) under two peaks, one for the low-voltage intercalation feature and one for the hydrogen-type feature at ~0.5 V vs Li/Li^+. Further details related to the estimation of the site type distributions shown in **Figure 3e** are given in the Supporting Information. From this analysis, two summarizing discoveries about Cor800 are clear: its reversible lithiation capacity cannot be explained by its surface area alone (as shown by the low contribution to capacity from surface adsorption) and that the novel hydrogen-type feature unique to Cor800 persists up to extremely fast lithiation/delithiation rates, even continuing to dominate the overall charge storage mechanism at 60 C. The content of H-type sites in Cor800, almost constant up to 40 C, corresponds to a lithium storage density of ~6.7 mmol g^{-1} or a stoichiometry of roughly $LiH_{2.4}C_{12}$. This remarkable capacity of high-power sites is highly relevant for next-generation LIBs since, unlike for the dominantly capacitive materials such as Super P and ZTC, Cor800 exhibits a relatively high first-cycle Coulombic efficiency of 55% and therefore low irreversible capacity loss that is often prohibitive for high-rate carbon materials. This fact is consistent with our proposed description of Cor800 containing an abundance of internal “hydrogen-type” sites within its bulk that are inaccessible to solvent but still readily lithiable up to ultrahigh current rates. We further propose that the predominance of such sites can be attributed to the imperfect tiling of the 2D plane by the large coronene precursor used to derive Cor800, leading to the formation of pockets where lithium could be trapped in a confined state between H-terminations, a feature not observed in equivalent materials derived from smaller PAHs (see Supporting Information). This lends a rich series of testable hypotheses that can guide future research into the use of PAHs of varying shape and symmetry toward further optimization of the content and characteristic potential of lithiation of H-type sites.

CONCLUSIONS

A novel type of lithiation mechanism of carbon materials has been observed and thoroughly characterized for a coronene-derived graphitic carbon material pyrolyzed at 800 °C referred to herein as

Cor800. This material is graphitic in nature and exhibits a low surface area akin to graphite. However, it also contains a high content of hydrogen in its elemental composition, implying an extensive edge character embedded within the bulk of the material (not accessible to the N_2 surface area analysis probe). The unique combination of wide interlayer graphitic stacking and internal hydrogen-type sites allows for rapid insertion and de-insertion of lithium at current rates up to 60 C (1 min charging time) with excellent reversibility and stability at ~0.5 V vs. Li/Li^+. The buried nature of these lithiation sites renders them protected from solvent during the first cycle lithiation, resulting in minimal SEI formation and therefore promising technological relevance. Whether such hydrogen-type sites can also be sodiated or potassiated in a similar way remains unknown and will be the focus of future work.[35]

EXPERIMENTAL SECTION

Materials Synthesis. Cor800 was synthesized by the direct pyrolysis of coronene (Acros Organics, 95%) under inert conditions at 800 °C. ZTC was synthesized via a two-step method, where dry NaY zeolite template (4 g, HSZ 320NAA, Tosoh Corp.) was first impregnated with liquid furfuryl alcohol (FA, 99%, Aldrich) and polymerized at 80 °C, followed by deposition of carbon by flowing 7 mol% propylene in argon (99.99% propylene in 99.999% argon) at 700 °C; finally, the product was annealed at 900 °C. The zeolite template was then removed by dissolution in aqueous hydrofluoric acid (HF, 48-51%, Thermo Scientific) and the product dried in air at 40 °C. Further synthetic details on PAH pyrolysis and ZTC synthesis can be found in the Supporting Information.

Commercial Reference Materials. Two commercially available reference materials were investigated in this study: AG20, a type of artificial graphite (synthetic graphite 282863, nominal particle size: <20 μm, Sigma-Aldrich) and Super P, a type of hard carbon commonly used as a conductive additive (supplied by Timcal Ltd.).

Materials Characterization. Powder XRD diffraction patterns were obtained from hand ground samples using a powder diffractometer (D8 ADVANCE, Bruker) in reflection geometry, equipped with a Cu $K\alpha_{1,2}$ radiation source (λ = 1.54 Å). Raman spectra were measured with a Raman spectrometer (LabRAM HR Evolution, Horiba Scientific Ltd.) equipped with a confocal microscope and a 532 nm (2.33 eV) frequency-doubled Nd:YAG laser operating at 45 mW. Scanning electron microscopy (SEM) of the as-synthesized materials was performed using a field emission scanning electron microscope (SUPRA 55VP, ZEISS Group) operating at 1 kV with a working distance of <5 mm. Samples were prepared by mounting onto conductive carbon tape. Surface area was determined via N_2 adsorption measurements performed using a volumetric Sieverts apparatus (3Flex, Micromeritics Corp.) at ~77 K; the data were fitted to a Brunauer-Emmett-Teller (BET) model following standard consistency criteria to yield the BET surface area (BET SA). Elemental analysis was determined by flame combustion (Atlantic Microlab, Inc.). Extensive experimental details as well as data analysis methods for XRD, Raman spectroscopy, N_2 adsorption, and elemental analysis can be found in the Supporting Information.

Electrochemical Characterization. Working electrodes were cast onto copper foil from a slurry containing 80 wt.% active material, 10 wt.% Super P as the conductive additive, and 10 wt.% polyvinylidene fluoride (PVDF) as the binder. The active mass loading was 1.2-1.6 mg cm^{-2}. Lithium half-cells were then assembled under inert argon conditions, comprising a lithium metal chip (MTI Corp.) as the counter/reference electrode, a glass microfiber separator (GF/D grade, catalogue number 1823–257, Whatman), and a working electrode (⌀ 10 mm) within a coin-type cell (316 stainless steel, size 2032, Xiamen AOT Electronics Technology Co.). Prior to sealing, the cell was charged with 125 µL of 1.2 M lithium hexafluorophosphate ($LiPF_6$) in a 3:7 by weight mixture of ethylene carbonate and ethyl methyl carbonate (with 2 wt.% fluoroethylene carbonate additive) as the electrolyte. GCD profiles were measured using a battery cycler (CT30001A, Landt Instruments). CV was performed on fresh cells using a potentiostat

(VersaSTAT 4-450, Princeton Applied Research). Further details can be found in the Supporting Information.

ASSOCIATED CONTENT

Supporting Information: Supporting Information is available free of charge at https://pubs.acs.org/. Synthesis details, materials characterization and analysis, electrode and cell fabrication details, electrochemical characterization and analysis, and systematic studies of smaller PAH-derived carbons.

Acknowledgments: We are very grateful to Harish Banda for insightful discussions. We also thank Erin Taylor for synthesis of the ZTC and Dalton Compton for performing the N_2 adsorption experiments. Funding for this work was provided by the DEVCOM Army Research Laboratory (ARL) under cooperative agreement (W911NF-20-2-0284). We also thank the Center for Biofilm Engineering Imaging Facility for use of their instrumentation, which is supported by funding from the National Science Foundation (DBI-1726561) and the M. J. Murdock Charitable Trust (SR-2017331).

References:

(1) *Lithium-Ion Batteries: Science and Technology*; Yoshio, M., Brodd, R. J., Kozawa, A. Eds.; Springer: New York, 2009.

(2) Yoshino, A. The Birth of the Lithium-Ion Battery. *Angew. Chem. Int. Ed.* **2012**, *51* (24), 5798–5800. https://doi.org/10.1002/anie.201105006.

(3) Nelson, P. A.; Ahmed, S.; Gallagher, K. G.; Dees, D. W. Modeling the Performance and Cost of Lithium-Ion Batteries for Electric-Drive Vehicles, Third Edition. **2019**. https://doi.org/10.2172/1503280.

(4) Wu, Y. P.; Jiang, C.; Wan, C.; Holze, R. Modified Natural Graphite as Anode Material for Lithium Ion Batteries. *J. Power Sources* **2002**, *111* (2), 329–334. https://doi.org/10.1016/S0378-7753(02)00349-X.

(5) von Lüders, C.; Zinth, V.; Erhard, S. V.; Osswald, P. J.; Hofmann, M.; Gilles, R.; Jossen, A. Lithium Plating in Lithium-Ion Batteries Investigated by Voltage Relaxation and in Situ Neutron Diffraction. *J. Power Sources* **2017**, *342*, 17–23. https://doi.org/10.1016/j.jpowsour.2016.12.032.

(6) Kim, D. S.; Kim, Y. E.; Kim, H. Improved Fast Charging Capability of Graphite Anodes via Amorphous Al2O3 Coating for High Power Lithium Ion Batteries. *J. Power Sources* **2019**, *422*, 18–24. https://doi.org/10.1016/j.jpowsour.2019.03.027.

(7) Xu, K. Nonaqueous Liquid Electrolytes for Lithium-Based Rechargeable Batteries. *Chem. Rev.* **2004**, *104* (10), 4303–4418. https://doi.org/10.1021/cr030203g.

(8) Persson, K.; Sethuraman, V. A.; Hardwick, L. J.; Hinuma, Y.; Meng, Y. S.; van der Ven, A.; Srinivasan, V.; Kostecki, R.; Ceder, G. Lithium Diffusion in Graphitic Carbon. *J. Phys. Chem. Lett.* **2010**, *1* (8), 1176–1180. https://doi.org/10.1021/jz100188d.

(9) Jow, T. R.; Delp, S. A.; Allen, J. L.; Jones, J.-P.; Smart, M. C. Factors Limiting Li^+ Charge Transfer Kinetics in Li-Ion Batteries. *J. Electrochem. Soc.* **2018**, *165* (2), A361–A367. https://doi.org/10.1149/2.1221802jes.

(10) Park, J. H.; Yoon, H.; Cho, Y.; Yoo, C.-Y. Investigation of Lithium Ion Diffusion of Graphite Anode by the Galvanostatic Intermittent Titration Technique. *Materials* **2021**, *14* (16), 4683. https://doi.org/10.3390/ma14164683.

(11) Weiss, M.; Ruess, R.; Kasnatscheew, J.; Levartovsky, Y.; Levy, N. R.; Minnmann, P.; Stolz, L.; Waldmann, T.; Wohlfahrt-Mehrens, M.; Aurbach, D.; Winter, M.; Ein-Eli, Y.; Janek, J. Fast Charging of Lithium-Ion Batteries: A Review of Materials Aspects. *Adv. Energy Mater.* **2021**, *11* (33), 2101126. https://doi.org/10.1002/aenm.202101126.

(12) Xu, W.; Welty, C.; Peterson, M. R.; Read, J. A.; Stadie, N. P. Exploring the Limits of the Rapid-Charging Performance of Graphite as the Anode in Lithium-Ion Batteries. *J. Electrochem. Soc.* **2022**, *169* (1), 010531. https://doi.org/10.1149/1945-7111/ac4b87.

(13) Dubey, R.; Zwahlen, M.; Shynkarenko, Y.; Yakunin, S.; Fuerst, A.; Kovalenko, M. V.; Kravchyk, K. V. Laser Patterning of High-Mass-Loading Graphite Anodes for High-Performance Li-Ion Batteries. *Batter. Supercaps* **2021**, *4* (3), 464–468. https://doi.org/10.1002/batt.202000253.

(14) Kottegoda, I. R. M.; Kadoma, Y.; Ikuta, H.; Uchimoto, Y.; Wakihara, M. High-Rate-Capable Lithium-Ion Battery Based on Surface-Modified Natural Graphite Anode and Substituted Spinel Cathode for Hybrid Electric Vehicles. *J. Electrochem. Soc.* **2005**, *152* (8), A1595. https://doi.org/10.1149/1.1948987.

(15) Yao, J.; Wang, G. X.; Ahn, J.; Liu, H. K.; Dou, S. X. Electrochemical Studies of Graphitized Mesocarbon Microbeads as an Anode in Lithium-Ion Cells. *J. Power Sources* **2003**, *114* (2), 292–297. https://doi.org/10.1016/S0378-7753(02)00585-2.

(16) Peng, C.; Liao, M. D.; Lv, X. L.; Chen, L.; Hou, S. P.; Min, D.; Chen, J.; Wang, H.-L.; Lin, J.-H. Large-Scale Synthesis of Highly Structural-Connecting Carbon Nanospheres as an Anodes Material for Lithium-Ion Batteries with High-Rate Capacity. *Chem. Eng. J. Adv.* **2020**, *2*, 100014. https://doi.org/10.1016/j.ceja.2020.100014.

(17) Yao, F.; Pham, D. T.; Lee, Y. H. Carbon-Based Materials for Lithium-Ion Batteries, Electrochemical Capacitors, and Their Hybrid Devices. *ChemSusChem* **2015**, *8* (14), 2284–2311. https://doi.org/10.1002/cssc.201403490.

(18) Dahn, J. R.; Zheng, T.; Liu, Y.; Xue, J. S. Mechanisms for Lithium Insertion in Carbonaceous Materials. *Science* **1995**, *270* (5236), 590–593. https://doi.org/10.1126/science.270.5236.590.

(19) Xing, W.; Xue, J. S.; Zheng, T.; Gibaud, A.; Dahn, J. R. Correlation Between Lithium Intercalation Capacity and Microstructure in Hard Carbons. *J. Electrochem. Soc.* **1996**, *143* (11), 3482–3491. https://doi.org/10.1149/1.1837241.

(20) Zheng, T.; Xing, W.; Dahn, J. R. Carbons Prepared from Coals for Anodes of Lithium-Ion Cells. *Carbon* **1996**, *34* (12), 1501–1507. https://doi.org/10.1016/S0008-6223(96)00098-X.

(21) Mathis, T. S.; Kurra, N.; Wang, X.; Pinto, D.; Simon, P.; Gogotsi, Y. Energy Storage Data Reporting in Perspective—Guidelines for Interpreting the Performance of Electrochemical Energy Storage Systems. *Adv. Energy Mater.* **2019**, *9* (39), 1902007. https://doi.org/10.1002/aenm.201902007.

(22) Enoki, T.; Miyajima, S.; Sano, M.; Inokuchi, H. Hydrogen-Alkali-Metal-Graphite Ternary Intercalation Compounds. *J. Mater. Res.* **1990**, *5* (2), 435–466. https://doi.org/10.1557/JMR.1990.0435.

(23) Zheng, T.; Liu, Y.; Fuller, E. W.; Tseng, S.; von Sacken, U.; Dahn, J. R. Lithium Insertion in High Capacity Carbonaceous Materials. *J. Electrochem. Soc.* **1995**, *142* (8), 2581–2590. https://doi.org/10.1149/1.2050057.

(24) Nishihara, H.; Kyotani, T. Zeolite-Templated Carbons – Three-Dimensional Microporous Graphene Frameworks. *Chem. Commun.* **2018**, *54* (45), 5648–5673. https://doi.org/10.1039/C8CC01932K.

(25) Taylor, E. E.; Garman, K.; Stadie, N. P. Atomistic Structures of Zeolite-Templated Carbon. *Chem. Mater.* **2020**, *32* (7), 2742–2752. https://doi.org/10.1021/acs.chemmater.0c00535.

(26) Ferrari, A. C.; Basko, D. M. Raman Spectroscopy as a Versatile Tool for Studying the Properties of Graphene. *Nat. Nanotechnol.* **2013**, *8* (4), 235–246. https://doi.org/10.1038/nnano.2013.46.

(27) McGlamery, D.; Baker, A. A.; Liu, Y.-S.; Mosquera, M. A.; Stadie, N. P. Phonon Dispersion Relation of Bulk Boron-Doped Graphitic Carbon. *J. Phys. Chem. C* **2020**, *124* (42), 23027–23037. https://doi.org/10.1021/acs.jpcc.0c06918.

(28) Diana, N.; Yamada, Y.; Gohda, S.; Ono, H.; Kubo, S.; Sato, S. Carbon Materials with High Pentagon Density. *J. Mater. Sci.* **2021**, *56* (4), 2912–2943. https://doi.org/10.1007/s10853-020-05392-x.

(29) Levi, M. D.; Aurbach, D. The Mechanism of Lithium Intercalation in Graphite Film Electrodes in Aprotic Media. Part 1. High Resolution Slow Scan Rate Cyclic Voltammetric Studies and Modeling. *J. Electroanal. Chem.* **1997**, *421* (1–2), 79–88. https://doi.org/10.1016/S0022-0728(96)04832-2.

(30) Peng, C.; Mercer, M. P.; Skylaris, C.-K.; Kramer, D. Lithium Intercalation Edge Effects and Doping Implications for Graphite Anodes. *J. Mater. Chem. A* **2020**, *8* (16), 7947–7955. https://doi.org/10.1039/C9TA13862E.

(31) Augustyn, V.; Come, J.; Lowe, M. A.; Kim, J. W.; Taberna, P.-L.; Tolbert, S. H.; Abruña, H. D.; Simon, P.; Dunn, B. High-Rate Electrochemical Energy Storage through Li+ Intercalation Pseudocapacitance. *Nat. Mater.* **2013**, *12* (6), 518–522. https://doi.org/10.1038/nmat3601.

(32) Gogotsi, Y.; Penner, R. M. Energy Storage in Nanomaterials – Capacitive, Pseudocapacitive, or Battery-Like? *ACS Nano* **2018**, *12* (3), 2081–2083. https://doi.org/10.1021/acsnano.8b01914.

(33) Fleischmann, S.; Mitchell, J. B.; Wang, R.; Zhan, C.; Jiang, D.; Presser, V.; Augustyn, V. Pseudocapacitance: From Fundamental Understanding to High Power Energy Storage Materials. *Chem. Rev.* **2020**, *120* (14), 6738–6782. https://doi.org/10.1021/acs.chemrev.0c00170.

(34) Simon, P.; Gogotsi, Y.; Dunn, B. Where Do Batteries End and Supercapacitors Begin? *Science* **2014**, *343* (6176), 1210–1211. https://doi.org/10.1126/science.1249625.

(35) Yin, J.; Jin, J.; Chen, C.; Lei, Y.; Tian, Z.; Wang, Y.; Zhao, Z.; Emwas, A.-H.; Zhu, Y.; Han, Y.; Schwingenschlögl, U.; Zhang, W.; Alshareef, H. N. Preferential Pyrolysis Construction of Carbon Anodes with 8400 h Lifespan for High-Energy-Density K-ion Batteries. *Angew. Chem. Int. Ed.* **2023**. https://doi.org/10.1002/anie.202301396.

TOC Image:

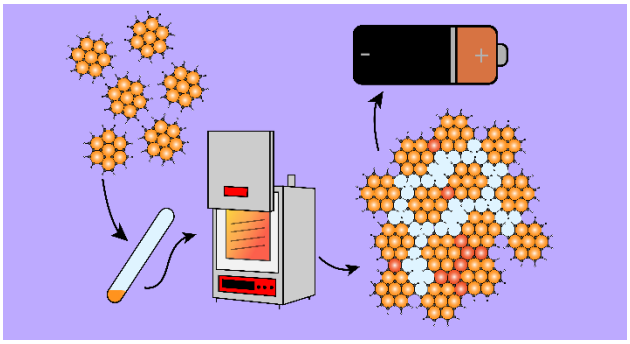

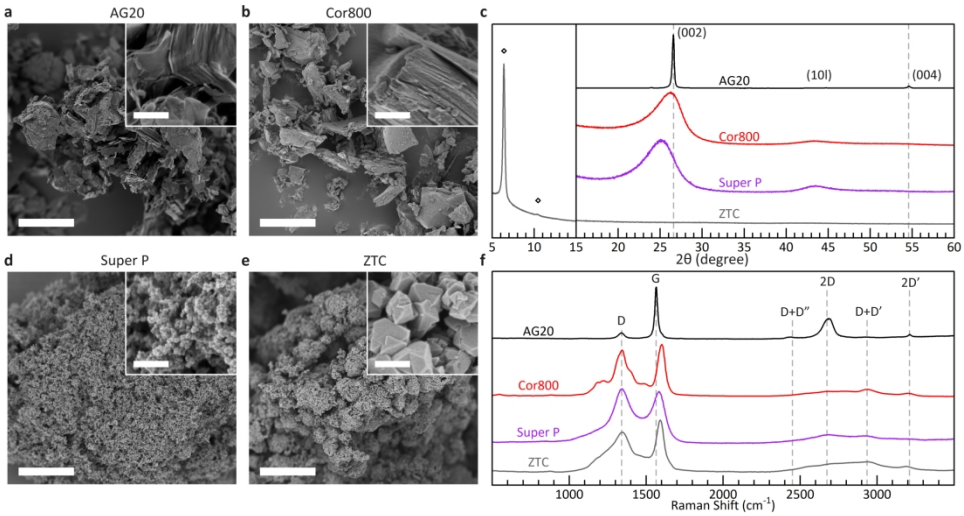

Figure 1. Representative SEM images of (a) graphite (AG20), (b) graphitic carbon with hydrogen-type sites (Cor800), (d) hard carbon (Super P), and (e) ordered porous carbon with no stacking (ZTC). The main image in each panel shows a 20 μm scale bar, and the inset shows a 500 nm scale bar. (c) XRD patterns of AG20, Cor800, Super P, and ZTC with the graphite (002) and (004) reflections indicated as dashed gray lines. The (111) and (220) reflections characteristic of the cubic pore-to-pore ordering in ZTC are indicated with open diamonds. (f) Raman spectra of AG20, Cor800, Super P, and ZTC, collected using a 532 nm excitation source.

203x105mm (300 x 300 DPI)

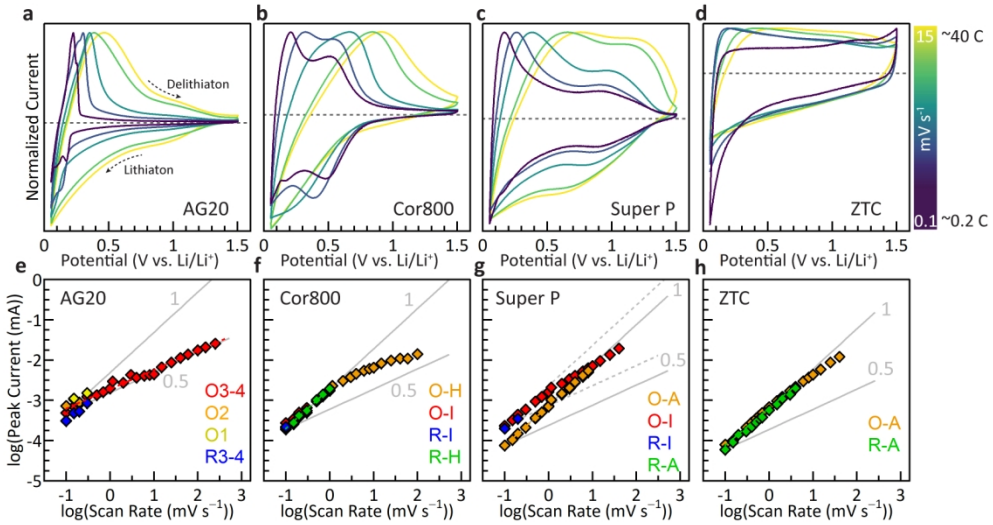

Figure 2. CV analysis of (a,e) AG20, (b,f) Cor800, (c,g) Super P, and (d,h) ZTC at scan rates between 0.1-15 mV s-1. (a-d) Select CV profiles and (e-h) R-S analysis showing the presence of numerous lithiation environments: reductive stage 3-4 intercalation (R3-4), wide interlayer intercalation (R-I), hydrogen-type site binding (R-H), and adsorption (R-A), and oxidative stage 1, 2, or 3-4 intercalation (O1, O2, and O3-4), wide interlayer intercalation (O-I), hydrogen-type site binding (O-H), and adsorption (O-A).

152x78mm (300 x 300 DPI)

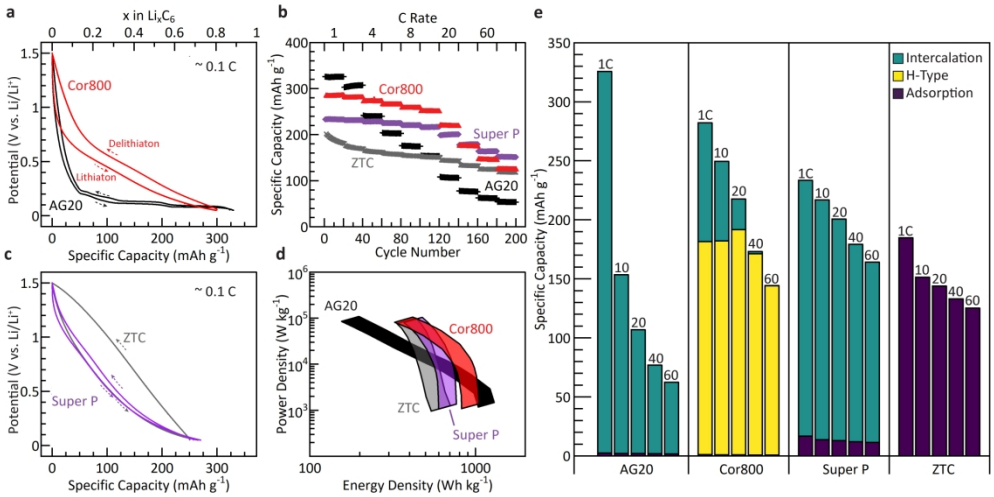

Figure 3. (a, c) Reversible GCD profiles of (a) AG20 and Cor800, and (c) Super P and ZTC at 25 mA g-1 (~0.1 C). (b) Cycling stability and rate capability of all materials at current rates between 0.4-30 A g-1 (~1-80 C, as shown). (d) Materials-specific Ragone plot assuming use of an anode against a range of standard cathodes (see Supporting Information for details). (e) Allocation of reversible charge storage capacity in all materials as per the type of lithiation environment (indicated by color) as a function of charging rate at select rates of 1 C, 10 C, 20 C, 40 C, and 60 C (indicated above each bar).

188x93mm (300 x 300 DPI)

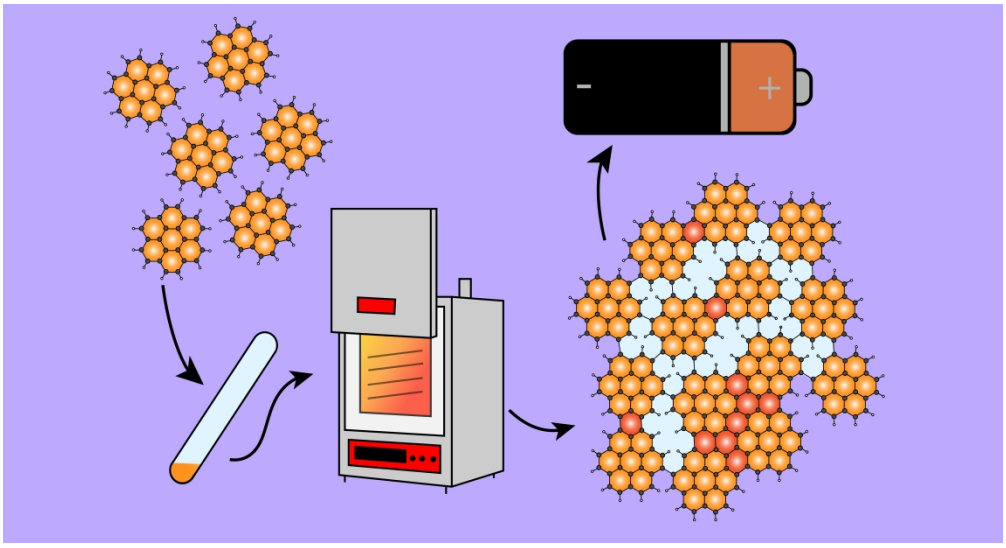

TOC Image

1473x793mm (96 x 96 DPI)